

Observations and analysis of an urban boundary layer and sea breezes during extreme heat events

Gabriel Rios ^{1*}, ^{2*}, Prathap Ramamurthy ^{1, 2}

1. Department of Mechanical Engineering, CUNY City College, New York, New York
2. NOAA Center for Earth System Sciences and Remote Sensing Technologies, New York, New York

Corresponding author: Gabriel Rios (grios001@citymail.cuny.edu)

*** Current affiliation(s):** Department of Mechanical Engineering, CUNY City College, New York, New York; NOAA Center for Earth System Sciences and Remote Sensing Technologies, New York, New York

For submission to the Quarterly Journal of the Royal Meteorological Society.

Last updated: February 16, 2022.

¹ Abstract

² Extreme heat presents a significant risk to human health and infrastructure in cities. Several studies
³ have been conducted in the past several decades to understand the interaction between the synoptic-
⁴ scale extreme heat events and local-scale urban heat island effects. However, observations of boundary
⁵ layer characteristics during these periods have been relatively rare. Our current understanding of urban
⁶ boundary layer structure is incomplete, particularly in coastal environments where the local climatology
⁷ is highly influenced by land-sea thermal gradients. In this study, we analyze the evolution and structure of
⁸ the urban boundary layer during regular and extreme heat periods with the goal of better understanding
⁹ the effect of extreme heat and sea breezes on the boundary layer over a coastal urban area. Our analysis
¹⁰ focuses on the New York City metropolitan area and relies on observations from vertical profilers (Doppler
¹¹ lidar, microwave radiometer) and quantities derived by analytical methods. Additionally, satellite and
¹² reanalysis data are used to supplement observational data. Extreme heat events present a mean peak
¹³ surface temperature increase of 7K, an increase of site-averaged specific humidity at the surface by
¹⁴ 39.4%, and a marked southwesterly shift in winds at all sites. In addition, sea breeze events during
¹⁵ heat extreme heat events are found to reduce temperatures and increase low-level moisture content from
¹⁶ the early evening through nighttime hours, with strong variability between sites. The study also finds
¹⁷ that extreme heat events unify horizontal wind directions throughout the boundary layer, and promote
¹⁸ nocturnal onshore moisture transport.

¹⁹ 1 Introduction

²⁰ Extreme heat poses a major risk to life and property. The effects of extreme heat are expected to
²¹ impact cities especially, which presents a significant hazard for vulnerable populations and infrastructure.
²² With regards to effects on public health, studies have shown that extreme and prolonged heat increases
²³ mortality and exacerbates existing health conditions in high-risk populations (Anderson and Bell, [2011](#);
²⁴ Frumkin, [2016](#); Heaviside, Macintyre, and Vardoulakis, [2017](#); Madrigano et al., [2015](#)). With regards to
²⁵ effects on infrastructure, studies have shown that extreme heat subjects networks critical to urban areas
²⁶ (e.g., electrical grid, public transportation) under significant stresses and/or failure (McEvoy, Ahmed,
²⁷ and Mullett, [2012](#); Zuo et al., [2015](#)). These events are projected to increase in frequency due to the effects
²⁸ of climate change. Projections indicate that the impacts of future climate will cause adverse effects of
²⁹ extreme heat to become more frequent and severe (Burillo et al., [2019](#); Forzieri et al., [2018](#); Peng et al.,
³⁰ [2011](#)).

31 The meteorology of extreme heat events and its impacts on urban areas can be observed from the synoptic
32 and local scales. From a synoptic scale, extreme heat events are often caused by the sustained presence of
33 a high-pressure system over an area, resulting in lower wind speeds and warm air subsidence, promoting
34 higher surface temperatures (Black et al., 2004; Miralles et al., 2014). From a local perspective, the
35 amplified impact of extreme heat events on cities is a result of the urban heat island (UHI) effect,
36 which occurs as a result of the modification of land surface properties due to the built environment.
37 The modification of surface properties has been shown to increase near-surface air temperatures due to
38 factors such as radiation entrapment, increased heat storage, and lower evapotranspirative cooling (F.
39 Chen, Yang, and Zhu, 2014; Dan Li and Elie Bou-Zeid, 2013; Ramamurthy and Bou-Zeid, 2017; Zhao
40 et al., 2018). Additionally, urban areas near large bodies of water experience effects from the sea breeze,
41 which has been shown to play a moderating influence on the intensity of the UHI effect (Hu and Xue,
42 2016; Jiang et al., 2019; Stéfanon et al., 2014). The processes on these two scales can be connected by
43 understanding the structure and dynamics of the urban boundary layer (UBL), which is the lowest part
44 of the troposphere in which surface-atmosphere exchanges occur that directly affect human activity.

45 There have been a large number of numerical studies performed to improve our understanding of UBL
46 processes during extreme heat events, which have been important for conceptualizing the role of synoptic-
47 scale and surface forcings on urban climate. Additionally, numerical models allow for the resolution of
48 spatial gaps that exist in many observational networks, particularly those in areas with heterogeneous
49 surface properties (such as urban areas). Among the numerous studies that accomplish this, many recent
50 papers have focused on the UBL over New York City. Meir et al. (2013) and Thompson, Holt, and Pullen
51 (2007) used numerical models to investigate various facets of the urban heat island and its interaction
52 with Atlantic sea breezes over New York City, which allowed for high-resolution simulations of conditions
53 and dynamics in a coastal urban area with complex land cover properties. Moreover, Bauer (2020)
54 investigated these factors in the vertical using the Weather Research and Forecasting (WRF) model,
55 allowing for a general visualization of the effects of roughness elements (such as supertall skyscrapers)
56 on UBL dynamics. Ramamurthy and Bou-Zeid (2017) used a sophisticated urban canopy model as an
57 addition to the WRF model to improve model representations of energy transfer into the UBL and its
58 effects on the UHI effect, whereas Ortiz et al. (2018) also used the WRF model with an urban canopy
59 parameterization and a building energy model to provide a more in-depth analysis of the UBL vertical
60 structure during extreme heat events.

61 Despite the significant progress made in researching UBL phenomena at multiple scales, observations of
62 the UBL are critical for answering several open questions in the field, validating results from numerical
63 simulations across a range of environments, and for serving as inputs and validation datasets to high-
64 resolution numerical weather models (Barlow, 2014; Best, 2005; Edwards et al., 2020; Leroyer et al., 2014;
65 Ronda et al., 2017). However, detailed observational analyses of UBL structure and dynamics are some-
66 what limited, especially in the vertical direction. These observations in the UBL have been limited, in
67 part, due to the lack of availability of remote sensing instruments that can observe UBL properties with a
68 sufficient spatiotemporal resolution (Barlow, 2014; Davis, Rajeev, and Sambhu Namboodiri, 2021; Roth,
69 2000; Y. Zhang et al., 2020) Over the last 20 years, microwave radiometers, lidars, and radiosondes have
70 been shown to be essential for accomplishing this. Microwave radiometers have been used to determine
71 vertical profiles of temperature and water vapor (Rose et al., 2005; Z. Wang et al., 2012), while lidars
72 being used to observe three-dimensional wind fields and aerosol concentrations (Grund et al., 2001).
73 Although radiosondes provide direct measurements of the aforementioned properties in the boundary
74 layer as it moves vertically through it, they present greater difficulties (e.g., cost, shorter supply) and
75 are unable to observe at the temporal resolution of microwave radiometers and lidars.

76 Although somewhat limited in spatiotemporal scale, numerous observational campaigns have been per-
77 formed to better our understanding of UBL structure and dynamics. Barlow et al. (2011) provides an
78 in-depth study of boundary layer dynamics above London over a month-long period using a combination

80 of a sonic anemometer and Doppler lidar, allowing for high-resolution vertical observations of a complex
81 UBL and a better understanding of turbulent structures and vertical mixing processes. Similarly, Pel-
82 liccioni et al. (2012) employs a sonic anemometer and a sodar system at a site in Rome to observe and
83 analyze the lower 200 m of the UBL to determine UBL characteristics and explore the validity of Monin-
84 Obukhov similarity theory in the surface layer. Additionally, Arruda Moreira et al. (2020) evaluates the
85 ability of lidar and microwave radiometer systems to observe turbulence over a variety of atmospheric
86 conditions, including the effects of significant dust concentrations, in the region around Granada, Spain.
87 Studies such as those performed by Banks et al. (2015), Quan et al. (2013), and Z. Wang et al. (2012)
88 further demonstrate the ability of vertical profiling instruments to analyze the boundary layer structure
89 by deriving UBL heights and its diurnal evolution. Expanding upon UBL structure, Anurose, Subra-
90 hamanyam, and Sunilkumar (2018) details a long-term observational campaign over an urban location
91 in southern India that chronicles UBL height through monsoon season, annual averages of near-surface
92 quantities, and the dynamics and effects of the sea breeze circulation.

93 Observations of the UBL during extreme heat events are even more limited. Ramamurthy and Bou-Zeid
94 (2017) used microwave radiometers to observe the UBL over New York City in July 2016 to find that
95 the UHI effect was amplified during heat wave events and that spatial variability throughout the city
96 was significant throughout the observation period. Jiang et al. (2019) explores the effects of heat waves
97 on rural and urban areas for several cities in China using ground-based observations with a focus on the
98 UHI effect, finding that the effect was amplified during heat waves due to greater surface solar radiation
99 and shifts in wind direction contributing to advection of heated air masses over the studied cities. (Wu
100 et al., 2019) uses a combination of a ceilometer and multiple lidars to observe the evolution of UBL
101 structure, air quality, and pollutant transport during a heat wave in New York City, demonstrating
102 sharp rates of UBL growth due to convective activity and an increase of pollutant concentration and
103 regional transport. Y. Zhang et al. (2020) uses aircraft-based observations to provide a comprehensive
104 analysis of UBL structure during heat wave events over cities in the United States throughout a 10-year
105 period, providing insights into the 'heat dome' thermodynamic structure over cities and the variability
106 between heat wave events due to local (such as surface properties in urban areas) and large-scale (such
107 as synoptic meteorological conditions) forcings.

108 New York City represents a complex case for urban meteorology given its diverse array of land cover types
109 (deciduous forest to supertall skyscrapers) and its proximity to multiple major bodies of water (Lower
110 New York Bay and the New York Bight to the south and east, Long Island Sound to the north and
111 east). Due to these factors, the effects of the surface energy budget (Hrisko, Prathap Ramamurthy, and
112 Gonzalez, 2021; Prathap Ramamurthy and Bou-Zeid, 2014; Tewari et al., 2019) and sea breezes (Childs
113 and Raman, 2005; Colle and Novak, 2010; Frizzola and Fisher, 1963; Gedzelman et al., 2003; Han et al.,
114 2022; Melecio-Vázquez et al., 2018; Thompson, Holt, and Pullen, 2007) on the mesoscale meteorology
115 have been studied extensively. However, similar to studies of other urban areas mentioned previously,
116 much of this research has involved numerical simulations of these meteorological processes. In this study,
117 we attempt to further our understanding of the UBL over a coastal urban area by compiling observations
118 from multiple locations within New York City and analyzing the UBL using derived quantities.

119 This study attempts to use observations and analytical methods to provide insight into the following
120 questions:

- 121 1. How do UBL structure and dynamics depart from the climatology during extreme heat events?
- 122 2. How do extreme heat events impact the transport of scalars?
- 123 3. What effect does the sea breeze have on a coastal urban area during extreme heat events?

124 **2 Data collection and analysis**

125 **2.1 Study site**

126 The UBL over New York City is observed and analyzed in this study. Observational data was captured
127 at four locations within New York City (Table 1).

Table 1: Locations and details of observations sites.

	Bronx	Queens	Staten Island
Coordinates	40.87248°N, 73.89352°E	40.73433°N, 73.81585°E	40.60401°N, 74.14850°E
Elevation (m a.g.l.)	57.8	56.3	32.4
Element roughness height (m a.g.l.)			
Valid wind directions	N/A	180 to 360°	N/A

Gabriel correct the tenses- some are present and some are in past.

Choose one and stick with it.

129 **2.2 Observational instruments**

130 Observations of the UBL were made using a synthesis of microwave radiometers, lidars, and satellites.

131

132 Vertical profiles of temperature and vapor density were captured using a network of Radiometrics
133 MP-3000A microwave radiometers (Hewison and Gaffard, 2003) operated by the New York State
134 Mesonet (Brotzge et al., 2020). Profiles for water vapor are retrieved using 21 channels in the 22-30.0
135 GHz (K-band) range, while profiles for temperature are retrieved using 14 channels in the 51-59.0 GHz
136 (V-band) range. Profile accuracy (relative to radiosonde soundings) determined by performance studies
137 at various locations reported an annually-averaged water vapor accuracy within 1.0 g m^{-3} below 2 km
138 and an annually-averaged temperature accuracy within 1.6 K below 4 km (Güldner and Spänkuch, 2001;
139 Sánchez et al., 2013). Quantities are captured at 58 height levels starting at ground level and ending
140 at 10 km above ground level, with vertical steps of 50 m from ground level to 500 m, 100 m from 500 m
141 to 2 km, and 250 m steps above 2 km. Observation integration times range from 0.01 to 2.50 s. Vertical
142 profiles are generated every 10 s and averaged over 10 min periods.

143

144 Wind measurements were measured using a network of Leosphere WindCube 100S Doppler lidars
145 operated by the New York State Mesonet (Brotzge et al., 2020). Measurements of wind motion using
146 the Doppler beam swinging scan mode in three directions: zonal (u), meridional (v), and vertical (w)
147 over 20 s cycles, with measurements averaged over 10 min intervals (Shrestha et al., 2021). The vertical
148 range of the WindCube 100S is 7 km above ground level with wind speed and direction accuracies of
149 0.5 m s^{-1} and 2° , respectively. The WindCube 100S has also been shown to perform with a high degree
150 of accuracy relative to radiosonde soundings, especially above 500 m (Kumer, Reuder, and Furevik, 2014).

151

152 Land and sea surface temperatures were estimated using derived products from the NOAA/NASA
153 GOES-16 Advanced Baseline Imager (ABI) (Ignatov et al., 2010; Yu et al., 2008). The GOES-16 ABI
154 provides a spatial resolution of 2 km with real-time data available to the public on an hourly basis.
155 The spatial extent of the Land Surface Temperature (LST) product ranges from the continental United
156 States (CONUS) to the majority of the Western Hemisphere (known as *full disk*), whereas the Sea
157 Surface Temperature (SST) product has a full disk spatial extent. The LST product has been found
158 to have an error relative to surface observations of 2.5 K over all land cover types, while sea surface
159 temperatures (SSTs) estimated using the GOES-16 ABI have been found to have an error relative to
160 shipborne radiometers $\leq 1 \text{ K}$ in the New York Bight (Luo and Minnett, 2021).

161 **2.2.1 Data criteria & availability**

162 Dates selected for this study are categorized into three groups: (1) normal days, (2) extreme heat days,
163 and (3) sea breeze days. For the purposes of this study, *extreme heat events* are defined as 3 or more
164 consecutive days with maximum daily temperatures exceeding 90°F (305 K), per the New York branch
165 of NOAA National Weather Service (Robinson, 2001; National Weather Service, 2018), while *normal*
166 *days* are defined as days that do not meet these criteria. Because the aim of this study is to observe the
167 effect of extreme heat on the UBL, normal day selection was restricted to months in which extreme heat
168 events occurred (May through September), as well as days in which 50% or more of the day featured
169 clear-sky conditions below 3.65 km above ground level due to the association of extreme heat events
170 with reduced daytime cloud coverage and precipitation (Stéfanon et al., 2014; Thomas et al., 2020).
171 Clear-sky conditions were identified by using an average of 5-minute surface-based observations from
172 three airports in the Automated Surface Observation System (ASOS) (NOAA et al., 1998) network
173 within the New York City metropolitan area: Newark Liberty International Airport (EWR), John F.
174 Kennedy International Airport, and LaGuardia Airport. *Sea breeze events* are identified as times during
175 normal and extreme heat days in which the low-level (≤ 200 m) mean horizontal wind speed (U) is less
176 than 5 m s^{-1} and low-level wind direction has a primarily easterly component, due to the presence of
177 the Atlantic Ocean to the east of New York City.

178 Observations from 102 days classified as normal and 87 days classified as extreme heat days were
179 used for this study. The observation period lasted from June 2018 to September 2021 and days were
180 selected between the months of May and September, as described previously. Quality filtering was per-
181 formed for microwave radiometer and lidar data. For microwave radiometer data, the retrieval of vertical
182 profiles of brightness temperature (from which derived values, such as temperature and vapor density)
183 are obtained continuously through 7 km above ground level with bi-weekly tip calibrations to reset the
184 K-band (Shrestha et al., 2021). For lidar data, data with carrier-to-noise ratio (CNR) values below -27
185 dB were rejected (Kumer, Reuder, and Furevik, 2014; Shrestha et al., 2021) due to poor retrieval quality.

187 Microwave radiometer observation data are shown in Figure 3 for all sites at selected heights.
188 Observation counts ranged between 200 and 250 hourly observation counts per site per selected height,
189 with increased availability due to the robustness of the sensing method. The lower observation count at
190 Staten Island is due to intermittent hardware issues preventing observations or storage of observational
191 data. Lidar data observation counts (normal and extreme heat) are shown in Figure 4 for each site
192 at selected heights. The observation count averages between 100 and 200 for every hour at 100, 500,
193 and 1000 m with lower counts at 2000 m due to poor data availability because of increased scattering
194 and noise. Observation counts grouped by wind direction are shown in Figure 5 at all sites for selected
195 heights. At lower heights, wind directions influenced by local factors result in higher observation counts
196 from most directions with the exception of true northerly winds. As observation height increases,
197 synoptic-scale factors dominate the observation count, with most observed winds coming from the west
198 or southwest.

200 **2.3 Derived quantities**

201 **3 Normal and extreme heat boundary layer properties**

202 This section discusses the differences in boundary layer structure and properties between normal days
203 and extreme heat events. Results are presented from the averages over all identified normal and heat
204 event days.

205 **3.1 Temperature**

206 On average, extreme heat events increase the temperature at the surface, as expected (see Figure
207 7). This is consistent across all observed locations in New York City, with the extreme heat event
208 temperature exceeding normal temperatures by approximately $1-\sigma$ over the entire day. An increase in
209 the difference is observed during daytime hours, with the difference peaking in magnitude around 13:00
210 LST at the hottest time of day. The surface temperature variability is significantly lower during heat
211 events (average $\sigma = 1.77\text{K}$) than during normal temperatures (average $\sigma = 4.57\text{K}$). There is little
212 spatial variability between sites, with maximum average temperatures ranging from 305.65 K in Queens
213 to 306.63 K in the Bronx. It is worth noting that there are areas in New York City that are located
214 in more heavily urbanized areas than the observation sites (such as Midtown Manhattan and central
215 Brooklyn), so it is likely that certain areas within the city have higher maximum temperatures.

216

217 Above the surface, extreme heat events increase the temperature significantly over the lowest
218 3000 m of the troposphere (see Figure 6), with standardized anomalies of θ ranging from $\sigma = 0.99$
219 to 1.30. The largest temperature anomalies shift from the surface layer in the mornings to span the
220 entirety of the mixed layer. This is reflective of strong surface forcing resulting in convection through
221 the mixed layer, as indicated by the formation of a late morning superadiabatic layer at all locations
222 (Figures 8, 9, 10).

223

224 These vertical profiles of θ suggest a degree of spatial variability in the UBL exists between lo-
225 cations. One instance of this spatial variability is vertical mixing; the Bronx site appears to have
226 stronger vertical mixing as shown in Figure 8, as θ remains constant for a greater height than at
227 the Queens and Staten Island locations, indicating a deeper mixed layer. This phenomenon is more
228 pronounced during extreme heat events, as a distinct mixed layer is apparent in the Bronx during early
229 (12:00 LST) and late (18:00 LST) afternoon hours. While a deepened mixed layer during extreme heat
230 events is also visible for the other locations, the strength of vertical mixing in the Bronx is emphasized
231 by persistent afternoon instability as shown by negative $\frac{d\theta}{dz}$ values between 500 and 1000 m and a
232 superadiabatic surface layer and 12:00 and 18:00 LST. **Ref 1**

233 **3.2 Moisture**

234 On average, extreme heat events were found to increase the moisture at the surface, as indicated by
235 the diurnal profiles of specific humidity (q) (see Figure 12). This is also consistent across all observed
236 locations in New York City, with the extreme heat event temperature exceeding normal temperatures
237 by approximately $1-\sigma$ over the entire day. Although a distinct diurnal profiles exists (q decreases during
238 daytime hours), the diurnal range is smaller in magnitude than temperature. It is also worth noting
239 that the diurnal range is lower for Staten Island than for the Bronx or Queens, suggesting that degree of
240 urbanization has a negative correlation with the diurnal range of q . Similar to surface temperature, the
241 variability of q is significantly lower during heat events (average $\sigma = 2.14 \times 10^{-3} \text{ kg kg}^{-1}$) than during
242 normal temperatures (average $\sigma = 3.18 \times 10^{-3} \text{ kg kg}^{-1}$). Queens shows exceptional variability in q ,
243 which may be attributed to the location of the observation site, which is adjacent to Flushing Meadows
244 Corona Park (large open vegetated space), is surrounded by a medium-density urban area on all other
245 sides, and is approximately 4 km from Long Island Sound.

246

247 In the boundary layer, the positive q anomalies subside in magnitude between 300 and 600 m,
248 but increase significantly in the mixed layer, especially during the late morning and early afternoon for
249 all sites. As shown in Figure 11, the largest anomalies occur between 10:00 and 16:00 LST throughout
250 the mixed layer. With regards to spatial variation in q , Staten Island demonstrates a strong positive
251 anomaly overnight through the early morning near the surface, indicating elevated low-level moisture
252 transport during extreme heat events, whereas the Bronx and Queens demonstrate a similar phenomenon

253 with a lesser anomaly magnitude. All sites show significant positive q anomalies throughout the day,
254 with the strongest anomaly signal starting in the low-levels throughout the morning and transitioning to
255 the mixed later by mid-afternoon. This trend suggests that the increase in nocturnal low-level moisture
256 corresponds to increased UBL moisture content due to strong vertical mixing throughout the daytime.

257 Ref 2

258 This is supported by Figures 13, 14, 15, where vertical profiles of q across all locations show
259 markedly higher q values at the surface during extreme heat events with $\frac{dq}{dz}$ values increasing throughout
260 the morning in the mixed layer while low-level q values decrease, indicating vertical transport of moisture
261 and drier low-level conditions during peak insolation. The strong vertical mixing of q can be observed
262 at all sites, where late morning and early afternoon $\frac{dq}{dz}$ values are greater during extreme heat events
263 than normal days. An example can be seen in the Bronx, where $\frac{dq}{dz} > 0$, indicating very efficient vertical
264 moisture transport.

265 3.3 UBL dynamics

266 3.3.1 Horizontal winds

267 Extreme heat events coincided with an overall reduction of horizontal wind speeds (U) in the UBL
268 (Figure 16). More specifically, the magnitude of U during extreme heat events is similar in magnitude
269 to U during normal days with the exception of early morning hours and at upper levels of the UBL. As
270 shown in Figure 17, modest reductions in U ($-1.2 \leq \sigma \leq -0.4$) during extreme heat events are present
271 throughout the UBL from early to mid-morning, with little difference throughout the rest of the day
272 ($-0.4 \leq \sigma \leq 0.4$). Larger deviations between U values are present at the top of the UBL where synoptic
273 conditions become dominant.

274

275 Vertical profiles of U for normal and extreme heat events provide a more detailed view of the
276 differences in UBL structure. Across all sites, U is similar throughout the UBL overnight, afternoon,
277 and evenings. During early morning hours, however, extreme heat event U values decrease by 25
278 to 50% throughout the entire UBL (see Figures 18, 19, 20), although both event types present a
279 classical logarithmic wind profile, with surface friction effects present through 500 m. The reduction
280 in U during extreme heat events is likely due to the presence of an anticyclonic circulation that
281 suppresses the nocturnal low-level jet over New York City (T. C. Chen and Kpaeyeh, 1993). Another
282 phenomenon worth noting is the difference in U profiles above 2000 m; profiles of U during extreme
283 heat events are more consistent between sites and vertically than during normal days. This phe-
284 nomenon is the effect of synoptic meteorological conditions on U , as the UBL typically remains below
285 2500 m. During extreme heat events, anticyclonic conditions produce more consistent atmospheric con-
286 ditions relative to normal days, resulting in less variability between heat events than during normal days.

287

288 Extreme heat events result in a southwesterly shift in U throughout the UBL. This shift is present most
289 evidently closer to the surface, as shown in Figures 21, 22, and 23, with winds at 100 m coming primarily
290 from the southwest quadrant. Figure 22 shows that Queens also presents a secondary maximum with
291 winds approaching from the south, which suggests effects from the Atlantic sea breeze (effects from
292 the sea breeze will be further discussed in Section 4). At 1000 m, the directionality of prevailing winds
293 becomes more uniform between normal and extreme heat days, as winds primarily approach New York
294 City from the west-southwest. The disparity in wind directions between 100 and 1000 m suggests that
295 localized wind fields play a more significant role in UBL dynamics at lower levels whereas synoptic-scale
296 atmospheric conditions increasingly dominate with increasing height. Regardless, the uniformity of
297 wind direction during extreme heat relative to normal days indicates that synoptic-scale effects can
298 play a larger role at lower levels due to advection from the continent, especially with regards to thermal
299 advection that leads to the transport of heated inland air masses over New York City (Ramamurthy, Li,
300 and Bou-Zeid, 2017).

301 **3.3.2 Vertical motion**

302 On average, extreme heat events do not appear to produce significant changes in vertical velocity (w).
303 Figure 24 shows average diurnal profiles of w at all locations at 100 m above ground level, with similar
304 mean values throughout the day between normal days and extreme heat events. During extreme heat
305 events, however, the variability of w is less in the early morning hours and greater in the evening. This
306 phenomenon is also observed in vertical profiles of w at all locations as shown in Figures 26, 27, and
307 28. At all locations, overnight and morning profiles of w (0:00 and 6:00 LST) show significantly lower
308 variability in w throughout the UBL with similar magnitudes of mean w . Despite similar means and
309 deviations in the early afternoon (12:00 LST), evening profiles (18:00 LST) show significantly higher
310 variability in w below 500 m for all sites, with the Bronx showing this occurrence extend through the
311 UBL. The similarity in vertical profiles of w may be a result of a balance between large-scale subsidence
312 (due to the presence of high-pressure during extreme heat events) and the effects of increased surface
313 forcings during extreme heat events relative to normal days (Dong et al., 2018; D.-L. Zhang, Shou, and
314 Dickerson, 2009). **Gabriel, it would be good to pick a representative normal and heatwave day for
a site and plot contours of w with height on y axis and time on x axis to visualize
updrafts/downdrafts.**

315 **4 Effects of the sea breeze circulation**

316 Sea breezes in New York City occur as a result of land-sea temperature gradients from two arms of the
317 Atlantic Ocean; the New York Bight to the southeast and Long Island Sound to the northeast. Sea
318 breezes from both bodies increase the complexity of UBL dynamics over New York City due to the
319 coalescence of opposing fronts over a complex topography (Bornstein and Thompson, 1981). A typical
320 sea breeze event in New York City is defined by calm ambient low-level winds ($\leq 5 \text{ m s}^{-1}$, the formation
321 of a large land-sea temperature gradient in the mid- to late morning, strong late-morning thermals
322 that promote low-level convergence, and afternoon to early-evening onshore moisture transport and
323 reduction in surface air temperatures (especially in areas closest to the shore) (Childs and Raman, 2005;
324 Frizzola and Fisher, 1963; Gedzelman et al., 2003).

325
326 Sea breeze events occurred on approximately 56% of all days observed. The high frequency of
327 occurrence is attributable to low-level convergence due to the large land-sea temperature gradient that
328 is common during warmer months (Childs and Raman, 2005; Gedzelman et al., 2003; Thompson, Holt,
329 and Pullen, 2007), as days were chosen exclusively between May and September. Maximum land-sea
330 surface temperature differences during days with identifiable sea breeze events averaged at 12 K, with a
331 strong diurnal profile with the peak difference occurring around midday (see Figure 29). The frequency
332 of occurrence increases when observing days during extreme heat events, as the lack of a strong synoptic
333 wind allows for the sea breeze circulation to become dominant in the metropolitan area (Miller et al.,
334 2003).

335 **4.1 UBL structure during sea breeze events**

336 During normal days, observations show that the sea breeze reduces temperature and increases moisture
337 content throughout the UBL after 12:00 LST. In Figure 30, the standardized anomalies of θ between
338 normal days with and without a sea breeze are shown, averaged over all days on an hourly basis.
339 Overnight and in the early morning, positive anomalies of θ are present above the UBL ($\leq 1 \text{ km}$)
340 until mid-morning, with the Bronx having the most significant anomaly and Staten Island the least.
341 This suggests a decreasing degree of anomalous θ with decreasing urbanization. This anomaly pattern
342 coincides with a positive q anomaly trend in both the spatiotemporal aspect (peak anomaly occurs above
343 1 km before 8:00 LST) and the magnitude aspect (the Bronx has the most significant early morning
344 anomaly, Staten Island has the least). Later in the day, all sites observe a negative θ anomaly throughout
345 the UBL despite a negative q anomaly, indicating that sea breeze events during normal days coincide
346 with a cooler and drier daytime UBL before the onset of the sea breeze. Sea breeze effects become

347 apparent during the mid-afternoon with the presence of a significant negative θ and positive q anomaly
348 in the lower UBL, with Staten Island experiencing effects first (approximately 16:00 LST) and the Bronx
349 experiencing effects last (approximately 19:00 LST). It is worth noting that the q anomaly is weak-
350 est in the Bronx, which suggests that the sea breeze front weakens as it travels inland over New York City.
351

352 During extreme heat events, observations show that the sea breeze plays a moderating role on
353 surface conditions by reducing low-level temperatures and increasing low-level moisture content, similar
354 to phenomena observed during normal days. In Figure 32, the standardized anomalies of θ between
355 extreme heat days with and without a sea breeze are shown, averaged over all days. All sites shown
356 that extreme heat days with a sea breeze possess slightly higher values of θ in the mid-morning,
357 with significant low-level reduction in θ in the afternoon and evening. On average, the onset of the
358 low-level cooling occurs in Staten Island first at approximately 12:00 LST, with Queens following at
359 approximately 14:00 LST, and the Bronx at about 18:00 LST. This disparity in times appears to
360 represent the passage of the southeasterly sea breeze front through New York City, where the onset
361 time correlates with the distance from the New York Bight (Bornstein and Thompson, 1981). A similar
362 phenomenon is observed by the transport of q as shown in Figure 33, with drier conditions throughout
363 the UBL before 12:00 LST and increasing low-level moisture as the day progresses. With regards to
364 onset, q follows a similar pattern to θ in that the onset time is dependent from distance to the shore.
365 These anomalies present most significantly in the lowest 1000 m of the UBL after 12:00 LST, which
366 aligns with sea breeze circulation characteristics observed in Frizzola and Fisher (1963).

367 4.2 UBL dynamics during sea breeze events

368 Days with identifiable sea breeze events had lower U throughout the majority of the UBL, with the
369 most significant decreases during the nighttime, potentially due to the lessening of onshore flow due
370 to the reduction of the land-sea temperature gradient (Pullen et al., 2007), as shown in Figure 29.
371 Vertical motions, however, increased significantly in the Bronx and Queens during the late morning and
372 early afternoon, as shown in Figure 34. These anomalies indicate the increased presence of updrafts in
373 urbanized areas which contribute to low-level convergence, promoting onshore flow in the afternoon and
374 evening.

375
376 During extreme heat days with identified sea breeze circulations, easterly winds increase in fre-
377 quency in the lower levels of the UBL, as shown in Figures 35, 36, and 37. These winds are the result
378 of onshore flow from the New York Bight (southeasterly) and Long Island Sound (northeasterly).

379
380 During extreme heat days with sea breeze circulations, southeasterly winds increased in frequency
381 compared to all other directions at all locations. The occurrence frequency of southeasterly winds is
382 correlated with the distance between the observation site and the largest body of water in proximity
383 of the metropolitan area (Atlantic Ocean), as Staten Island reported 92.1% of all winds at 100 m as
384 southeasterly between 12:00 and 20:00 LST (distance of 6.50 km from Lower New York Bay), whereas
385 Queens reported 67.4% (distance of 16.5 km) and Bronx reported 55.6% (distance of 32.9 km) during
386 the same time interval. The disparity in southeasterly winds further demonstrates the spatial extent
387 and progression of the sea breeze front.

388
389 For sites near Long Island Sound (the Bronx and Queens), northeasterly winds increased in fre-
390 quency as well, though not to the same magnitude as southeasterly winds. This disparity in magnitude
391 suggests that the Long Island Sound sea breeze front is weaker than the New York Bight sea breeze
392 front, which aligns with previous studies of sea breeze fronts over New York City (Frizzola and Fisher,
393 1963; Meir et al., 2013). Northeasterly winds increased in frequency during extreme heat days with
394 sea breeze circulations, with a notable increase in the early morning hours (a likely result of nocturnal
395 low-level motion) and in the evening hours (signal of a Long Island Sound sea breeze). This phenomenon

396 is also apparent in Queens and Staten Island, albeit to a lesser frequency.

397 5 Conclusions

- 398 1. The UBL shows increased temperatures and moisture content throughout its entirety during ex-
399 treme heat events. Additionally, the UBL presents a more uniform structure due to increased
400 vertical mixing relative to normal days, especially in areas with higher degrees of urbanization.
- 401 2. Transport of scalars appears to increase in the vertical direction during extreme heat events in
402 the UBL, although decreased low-level horizontal winds suppresses strong scalar transport zonally
403 and meridionally.
- 404 3. The sea breeze reduces temperatures throughout the UBL after the onset of the sea breeze, which
405 typically occurs in the mid-afternoon in immediate coastal areas and in the evening for areas
406 further inland. The sea breeze also results in nocturnal low-level onshore moisture transport.

407 Acknowledgments

408 This research is made possible by the New York State (NYS) Mesonet. Original funding for the NYS
409 Mesonet was provided by Federal Emergency Management Agency grant FEMA-4085-DR-NY, with the
410 continued support of the NYS Division of Homeland Security & Emergency Services; the state of New
411 York; the Research Foundation for the State University of New York (SUNY); the University at Albany,
412 SUNY; the Atmospheric Sciences Research Center (ASRC) at SUNY Albany; and the Department of
413 Atmospheric and Environmental Sciences (DAES) at SUNY Albany. This research was also funded by
414 the Department of Defense Army Research Office Grant No. W911NF2020126.

415 References

- 416 Anderson, G Brooke and Michelle L Bell (2011). “Heat waves in the United States: mortality risk during heat
417 waves and effect modification by heat wave characteristics in 43 US communities”. In: *Environmental health
418 perspectives* 119.2, pp. 210–218.
- 419 Anurose, TJ, D Bala Subrahmanyam, and SV Sunilkumar (2018). “Two years observations on the diurnal
420 evolution of coastal atmospheric boundary layer features over Thiruvananthapuram (8.5° N, 76.9° E), India”.
421 In: *Theoretical and applied climatology* 131.1, pp. 77–90.
- 422 Arruda Moreira, Gregori de et al. (2020). “Study of the planetary boundary layer height in an urban environment
423 using a combination of microwave radiometer and ceilometer”. In: *Atmospheric Research* 240, p. 104932.
- 424 Banks, Robert F et al. (2015). “Performance evaluation of the boundary-layer height from lidar and the Weather
425 Research and Forecasting model at an urban coastal site in the north-east Iberian Peninsula”. In: *Boundary-
426 layer meteorology* 157.2, pp. 265–292.
- 427 Barlow, Janet F (2014). “Progress in observing and modelling the urban boundary layer”. In: *Urban Climate* 10,
428 pp. 216–240.
- 429 Barlow, Janet F et al. (2011). “Boundary layer dynamics over London, UK, as observed using Doppler lidar
430 during REPARTEE-II”. In: *Atmospheric Chemistry and Physics* 11.5, pp. 2111–2125.
- 431 Bauer, Timothy J (2020). “Interaction of urban heat island effects and land–sea breezes during a New York City
432 heat event”. In: *Journal of Applied Meteorology and Climatology* 59.3, pp. 477–495.
- 433 Best, MJ (2005). “Representing urban areas within operational numerical weather prediction models”. In:
434 *Boundary-Layer Meteorology* 114.1, pp. 91–109.
- 435 Black, Emily et al. (2004). “Factors contributing to the summer 2003 European heatwave”. In: *Weather* 59.8,
436 pp. 217–223.
- 437 Bornstein, Robert D and William T Thompson (1981). “Effects of frictionally retarded sea breeze and synoptic
438 frontal passages on sulfur dioxide concentrations in New York City”. In: *Journal of Applied Meteorology and
439 Climatology* 20.8, pp. 843–858.

- 440 Brotzge, Jerald A et al. (2020). "A technical overview of the new york state mesonet standard network". In:
441 *Journal of Atmospheric and Oceanic Technology* 37.10, pp. 1827–1845.
- 442 Burillo, Daniel et al. (2019). "Electricity infrastructure vulnerabilities due to long-term growth and extreme heat
443 from climate change in Los Angeles County". In: *Energy Policy* 128, pp. 943–953.
- 444 Chen, Feng, Xuchao Yang, and Weiping Zhu (2014). "WRF simulations of urban heat island under hot-weather
445 synoptic conditions: The case study of Hangzhou City, China". In: *Atmospheric research* 138, pp. 364–377.
- 446 Chen, T C and J Alvin Kpaeyeh (1993). "The synoptic-scale environment associated with the low-level jet of the
447 Great Plains". In: *Monthly weather review* 121.2, pp. 416–420.
- 448 Childs, Peter P and Sethu Raman (2005). "Observations and numerical simulations of urban heat island and sea
449 breeze circulations over New York City". In: *Pure and Applied Geophysics* 162.10, pp. 1955–1980.
- 450 Colle, Brian A and David R Novak (2010). "The New York Bight jet: climatology and dynamical evolution". In:
451 *Monthly Weather Review* 138.6, pp. 2385–2404.
- 452 Davis, Edwin V, K Rajeev, and KV Sambhu Namboodiri (2021). "The Convective-Atmospheric-Boundary-Layer
453 Height and its dependence upon Meteorological Variables At a Tropical Coastal Station during Onshore and
454 Offshore Flows". In: *Boundary-Layer Meteorology*, pp. 1–24.
- 455 Dong, Li et al. (2018). "The dynamical linkage of atmospheric blocking to drought, heatwave and urban heat
456 island in southeastern US: A multi-scale case study". In: *Atmosphere* 9.1, p. 33.
- 457 Edwards, John M et al. (2020). "Representation of boundary-layer processes in numerical weather prediction and
458 climate models". In: *Boundary-Layer Meteorology* 177.2, pp. 511–539.
- 459 Forzieri, Giovanni et al. (2018). "Escalating impacts of climate extremes on critical infrastructures in Europe".
460 In: *Global environmental change* 48, pp. 97–107.
- 461 Frizzola, John A and Edwin L Fisher (1963). "A series of sea breeze observations in the New York City area".
462 In: *Journal of Applied Meteorology and Climatology* 2.6, pp. 722–739.
- 463 Frumkin, Howard (2016). "Urban sprawl and public health". In: *Public health reports*.
- 464 Gedzelman, SD et al. (2003). "Mesoscale aspects of the urban heat island around New York City". In: *Theoretical
465 and applied climatology* 75.1, pp. 29–42.
- 466 Grund, Christian J et al. (2001). "High-resolution Doppler lidar for boundary layer and cloud research". In:
467 *Journal of Atmospheric and Oceanic Technology* 18.3, pp. 376–393.
- 468 Güldner, J and D Spänkuch (2001). "Remote sensing of the thermodynamic state of the atmospheric boundary
469 layer by ground-based microwave radiometry". In: *Journal of Atmospheric and Oceanic Technology* 18.6,
470 pp. 925–933.
- 471 Han, ZS et al. (2022). "Observed sea breeze life cycle in and around NYC: Impacts on UHI and ozone patterns".
472 In: *Urban Climate* 42, p. 101109.
- 473 Heaviside, Clare, Helen Macintyre, and Sotiris Vardoulakis (2017). "The urban heat island: implications for health
474 in a changing environment". In: *Current environmental health reports* 4.3, pp. 296–305.
- 475 Hewison, Tim and Catherine Gaffard (2003). "Radiometrics MP3000 microwave radiometer performance assess-
476 ment". In: *Obs. Development Technical Report TR29, Met Office, National Meteorological Library, Exeter,
477 UK. Also available from <http://tim.hewison.org/TR29.pdf>.*
- 478 Hrisko, Joshua, Prathap Ramamurthy, and Jorge E Gonzalez (2021). "Estimating heat storage in urban areas
479 using multispectral satellite data and machine learning". In: *Remote Sensing of Environment* 252, p. 112125.
- 480 Hu, Xiao-Ming and Ming Xue (2016). "Influence of synoptic sea-breeze fronts on the urban heat island intensity
481 in Dallas–Fort Worth, Texas". In: *Monthly Weather Review* 144.4, pp. 1487–1507.
- 482 Ignatov, A et al. (2010). "GOES-R Advanced Baseline Imager (ABI) algorithm theoretical basis document for
483 sea surface temperature". In: *NOAA NESDIS Center for Satellite Applications and Research*.
- 484 Jiang, Shaojing et al. (2019). "Amplified urban heat islands during heat wave periods". In: *Journal of Geophysical
485 Research: Atmospheres* 124.14, pp. 7797–7812.
- 486 Kumer, Valerie-M, Joachim Reuder, and Birgitte R Furevik (2014). "A comparison of LiDAR and radiosonde
487 wind measurements". In: *Energy Procedia* 53, pp. 214–220.
- 488 Leroyer, Sylvie et al. (2014). "Subkilometer numerical weather prediction in an urban coastal area: A case study
489 over the Vancouver metropolitan area". In: *Journal of Applied Meteorology and Climatology* 53.6, pp. 1433–
490 1453.
- 491 Li, Dan and Elie Bou-Zeid (2013). "Synergistic interactions between urban heat islands and heat waves: The
492 impact in cities is larger than the sum of its parts". In: *Journal of Applied Meteorology and Climatology* 52.9,
493 pp. 2051–2064.

- 494 Luo, Bingkun and Peter J Minnett (2021). "Skin Sea Surface Temperatures From the GOES-16 ABI Validated
495 With Those of the Shipborne M-AERI". In: *IEEE Transactions on Geoscience and Remote Sensing* 59.12,
496 pp. 9902–9913.
- 497 Madrigano, Jaime et al. (2015). "A case-only study of vulnerability to heat wave-related mortality in New York
498 City (2000–2011)". In: *Environmental health perspectives* 123.7, pp. 672–678.
- 499 McEvoy, Darryn, Iftekhar Ahmed, and Jane Mullett (2012). "The impact of the 2009 heat wave on Melbourne's
500 critical infrastructure". In: *Local Environment* 17.8, pp. 783–796.
- 501 Meir, Talmor et al. (2013). "Forecasting the New York City urban heat island and sea breeze during extreme
502 heat events". In: *Weather and Forecasting* 28.6, pp. 1460–1477.
- 503 Melecio-Vázquez, David et al. (2018). "Thermal Structure of a Coastal–Urban Boundary Layer". In: *Boundary-
504 Layer Meteorology* 169 (1), pp. 151–161. ISSN: 15731472.
- 505 Miller, STK et al. (2003). "Sea breeze: Structure, forecasting, and impacts". In: *Reviews of geophysics* 41.3.
- 506 Miralles, Diego G et al. (2014). "Mega-heatwave temperatures due to combined soil desiccation and atmospheric
507 heat accumulation". In: *Nature geoscience* 7.5, pp. 345–349.
- 508 National Weather Service, NOAA (May 2018). *National Weather Service New York, NY excessive heat page*. URL:
509 <https://www.weather.gov/okx/excessiveheat>.
- 510 NOAA et al. (1998). *Automated Surface Observing System (ASOS) User's Guide*. URL: <https://www.weather.gov/media/asos/aum-toc.pdf>.
- 511 Ortiz, Luis E et al. (2018). "New York City impacts on a regional heat wave". In: *Journal of applied meteorology
513 and climatology* 57.4, pp. 837–851.
- 514 Pelliccioni, A et al. (2012). "Some characteristics of the urban boundary layer above Rome, Italy, and applicability
515 of Monin–Obukhov similarity". In: *Environmental fluid mechanics* 12.5, pp. 405–428.
- 516 Peng, Roger D et al. (2011). "Toward a quantitative estimate of future heat wave mortality under global climate
517 change". In: *Environmental health perspectives* 119.5, pp. 701–706.
- 518 Pullen, Julie et al. (2007). "Atmospheric response to local upwelling in the vicinity of New York–New Jersey
519 harbor". In: *Journal of applied meteorology and climatology* 46.7, pp. 1031–1052.
- 520 Quan, Jiannong et al. (2013). "Evolution of planetary boundary layer under different weather conditions, and its
521 impact on aerosol concentrations". In: *Particuology* 11.1, pp. 34–40.
- 522 Ramamurthy, P and E Bou-Zeid (2017). "Heatwaves and urban heat islands: a comparative analysis of multiple
523 cities". In: *Journal of Geophysical Research: Atmospheres* 122.1, pp. 168–178.
- 524 Ramamurthy, P, D Li, and E Bou-Zeid (2017). "High-resolution simulation of heatwave events in New York
525 City". In: *Theoretical and applied climatology* 128.1, pp. 89–102.
- 526 Ramamurthy, Prathap and E Bou-Zeid (2014). "Contribution of impervious surfaces to urban evaporation". In:
527 *Water Resources Research* 50.4, pp. 2889–2902.
- 528 Robinson, Peter J (2001). "On the definition of a heat wave". In: *Journal of Applied Meteorology and Climatology*
529 40.4, pp. 762–775.
- 530 Ronda, RJ et al. (2017). "Urban finescale forecasting reveals weather conditions with unprecedented detail". In:
531 *Bulletin of the American Meteorological Society* 98.12, pp. 2675–2688.
- 532 Rose, Thomas et al. (2005). "A network suitable microwave radiometer for operational monitoring of the cloudy
533 atmosphere". In: *Atmospheric research* 75.3, pp. 183–200.
- 534 Roth, Matthias (2000). "Review of atmospheric turbulence over cities". In: *Quarterly Journal of the Royal Me-
535 teorological Society* 126.564, pp. 941–990.
- 536 Sánchez, JL et al. (2013). "A method to improve the accuracy of continuous measuring of vertical profiles of
537 temperature and water vapor density by means of a ground-based microwave radiometer". In: *Atmospheric
538 Research* 122, pp. 43–54.
- 539 Shrestha, Bhupal et al. (2021). "Overview and Applications of the New York State Mesonet Profiler Network".
540 In: *Journal of Applied Meteorology and Climatology* 60.11, pp. 1591–1611.
- 541 Stéfanon, Marc et al. (2014). "Soil moisture-temperature feedbacks at meso-scale during summer heat waves over
542 Western Europe". In: *Climate dynamics* 42.5, pp. 1309–1324.
- 543 Tewari, Mukul et al. (2019). "Interaction of urban heat islands and heat waves under current and future climate
544 conditions and their mitigation using green and cool roofs in New York City and Phoenix, Arizona". In:
545 *Environmental Research Letters* 14.3, p. 034002.
- 546 Thomas, Natalie P et al. (2020). "Mechanisms associated with daytime and nighttime heat waves over the
547 contiguous united states". In: *Journal of Applied Meteorology and Climatology* 59.11, pp. 1865–1882.

- 548 Thompson, William T, Teddy Holt, and Julie Pullen (2007). "Investigation of a sea breeze front in an urban envi-
 549 ronment". In: *Quarterly Journal of the Royal Meteorological Society: A journal of the atmospheric sciences,*
 550 *applied meteorology and physical oceanography* 133.624, pp. 579–594.
- 551 Wang, Z et al. (2012). "Lidar measurement of planetary boundary layer height and comparison with microwave
 552 profiling radiometer observation". In: *Atmospheric Measurement Techniques* 5.8, pp. 1965–1972.
- 553 Wu, Yonghua et al. (2019). "Observation of heat wave effects on the urban air quality and PBL in New York
 554 City area". In: *Atmospheric Environment* 218, p. 117024.
- 555 Yu, Yunyue et al. (2008). "Developing algorithm for operational GOES-R land surface temperature product". In:
 556 *IEEE Transactions on Geoscience and Remote Sensing* 47.3, pp. 936–951.
- 557 Zhang, Da-Lin, Yi-Xuan Shou, and Russell R Dickerson (2009). "Upstream urbanization exacerbates urban heat
 558 island effects". In: *Geophysical Research Letters* 36.24.
- 559 Zhang, Yuanjie et al. (2020). "Aircraft observed diurnal variations of the planetary boundary layer under heat
 560 waves". In: *Atmospheric Research* 235, p. 104801.
- 561 Zhao, Lei et al. (2018). "Interactions between urban heat islands and heat waves". In: *Environmental research
 562 letters* 13.3, p. 034003.
- 563 Zuo, Jian et al. (2015). "Impacts of heat waves and corresponding measures: a review". In: *Journal of Cleaner
 564 Production* 92, pp. 1–12.

565 Appendix

$$p = p_0 \exp \frac{-gz}{RT_0}$$

$$\theta = T \left(\frac{p_0}{p} \right)^{\frac{R}{c_p}}$$

$$q = \frac{w}{1+w} = \frac{\frac{\varepsilon \rho'_v R_v T}{p - \rho'_v R_v T}}{1 + \frac{\varepsilon \rho'_v R_v T}{p - \rho'_v R_v T}}$$

$$Ri_b = \frac{g \Delta \bar{\theta}_v \Delta z}{\bar{\theta}_v [(\Delta \bar{U}^2) + (\Delta \bar{V}^2)]}$$

Table 2: Symbols and abbreviations used in the paper.

Symbol/Abbreviation	Definition
σ	Standard deviation
θ	Potential temperature
q	Specific humidity
U	Horizontal wind speed
w	Vertical velocity
UBL	Urban boundary layer
MLH	Mixed layer height

567 Figures

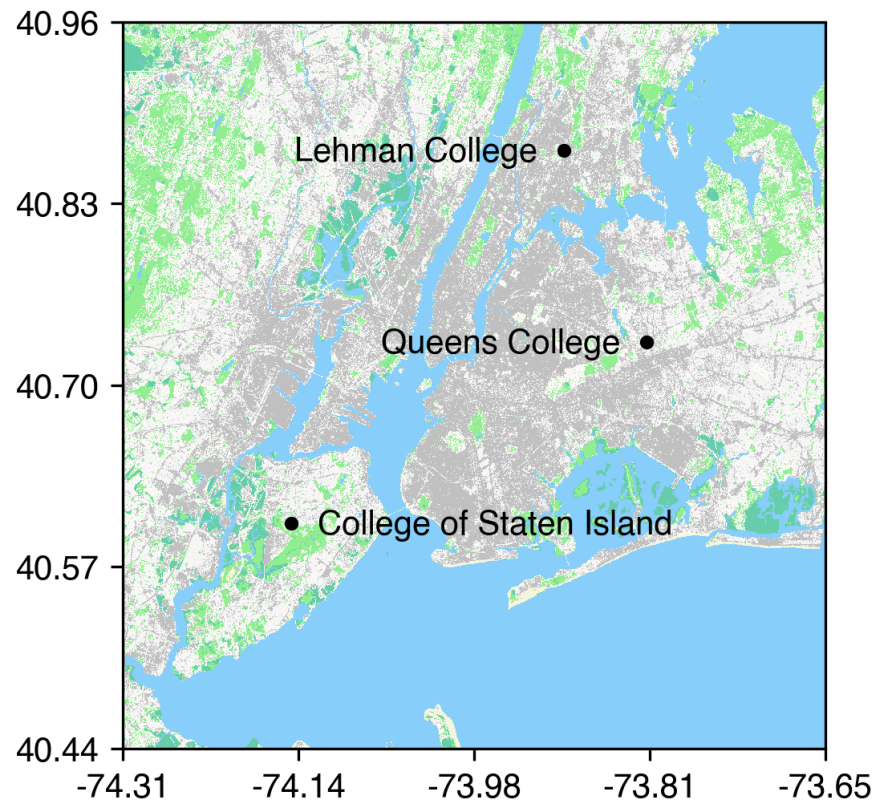


Figure 1: Observation sites overlaid on NLCD land cover types.

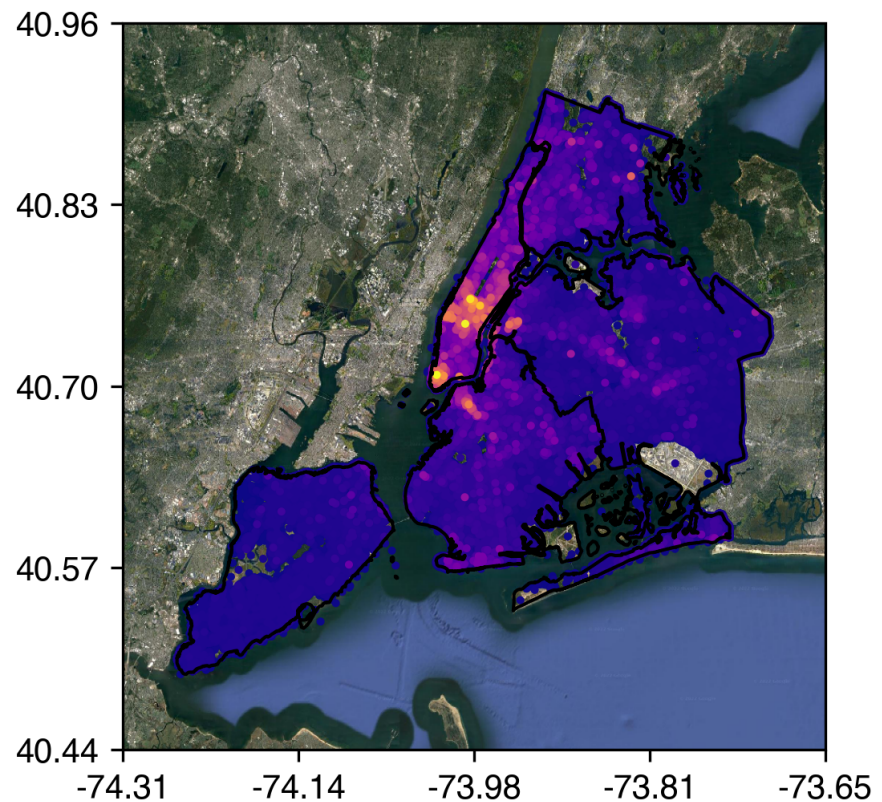


Figure 2: Building heights in New York City. Taken from NYC DOB data.

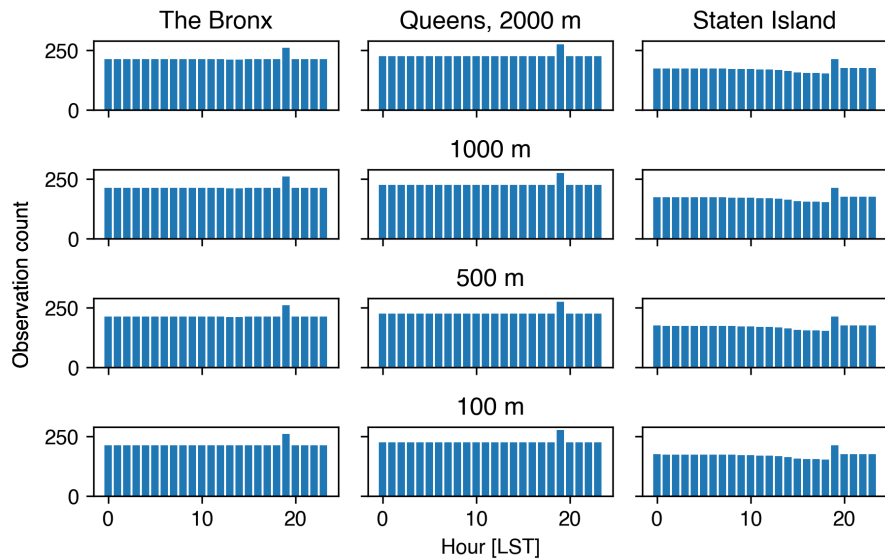


Figure 3: Microwave radiometer observation statistics for all sites at selected heights.

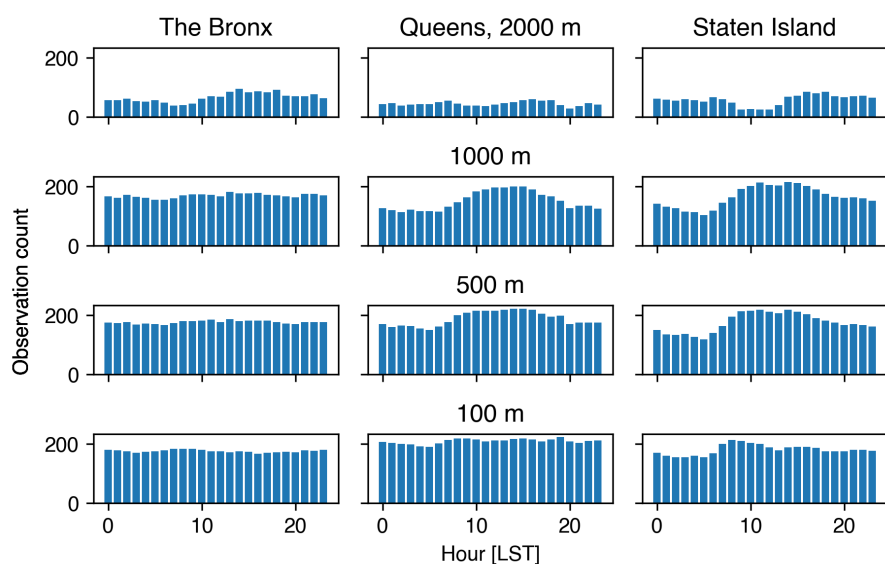


Figure 4: Lidar observation statistics for all sites at selected heights.

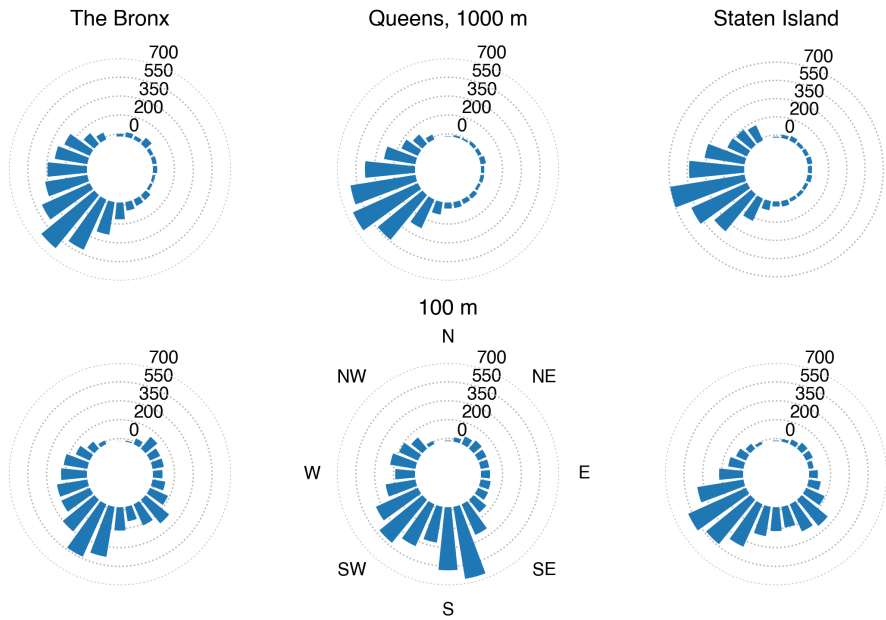


Figure 5: Wind direction observation statistics for all sites at selected heights.

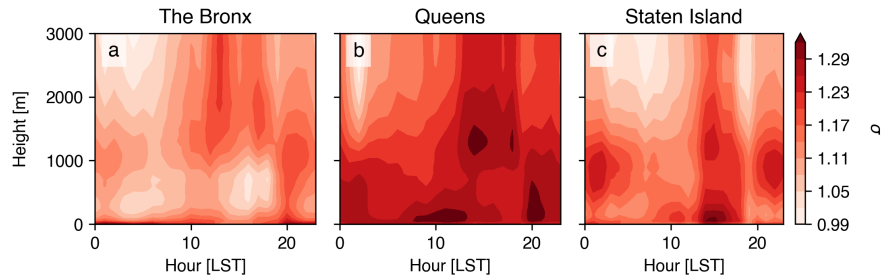


Figure 6: Anomalies of θ during extreme heat events relative to the climatology over the urban boundary layer.

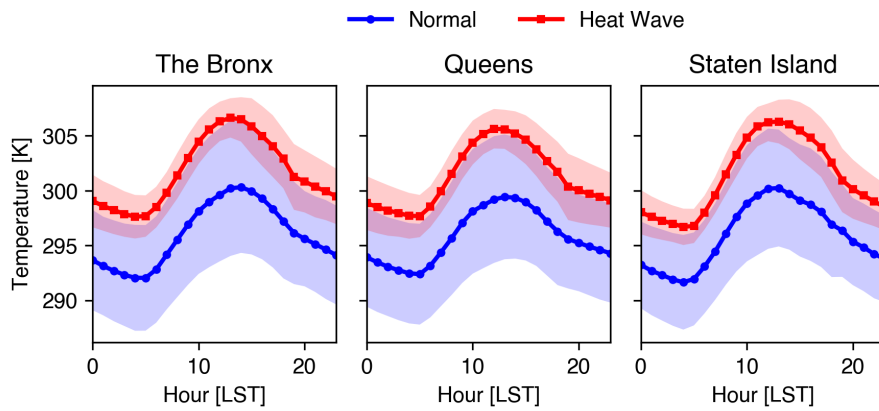


Figure 7: Anomalies of temperature during extreme heat events relative to the climatology at the surface.

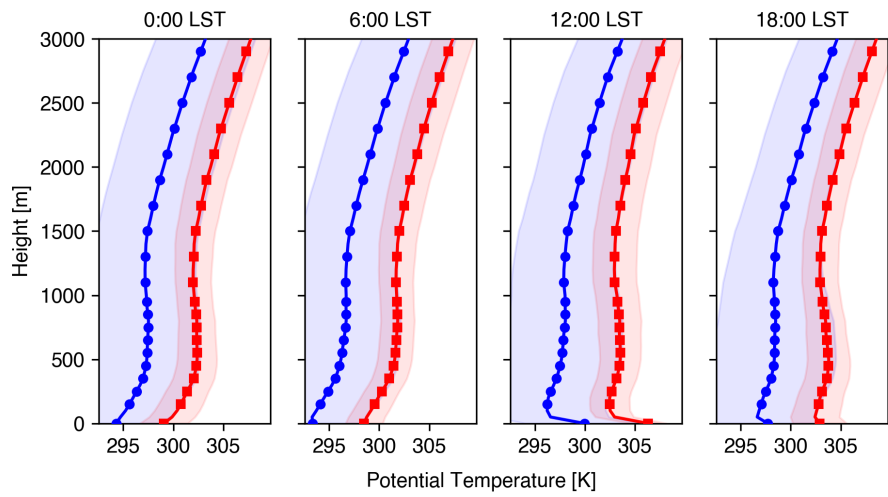


Figure 8: Vertical profiles of θ in the Bronx during normal days (blue) and extreme heat events (red).

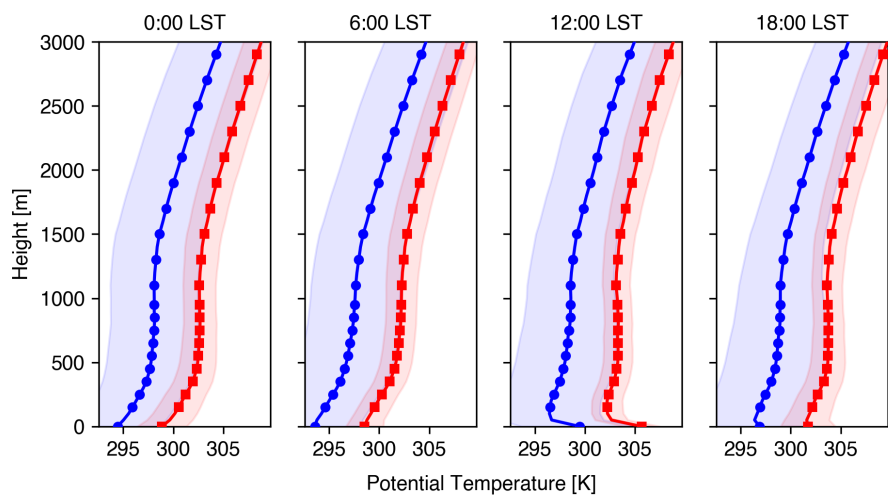


Figure 9: Vertical profiles of θ in Queens during normal days (blue) and extreme heat events (red).

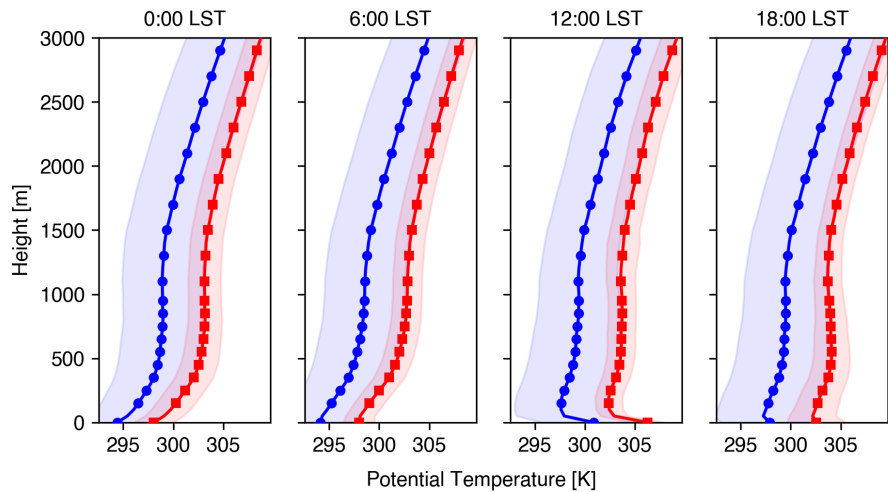


Figure 10: Vertical profiles of θ in Staten Island during normal days (blue) and extreme heat events (red).

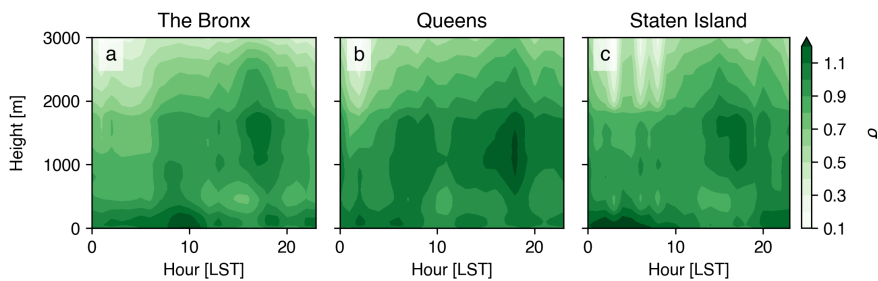


Figure 11: Anomalies of q during extreme heat events relative to the climatology over the urban boundary layer.

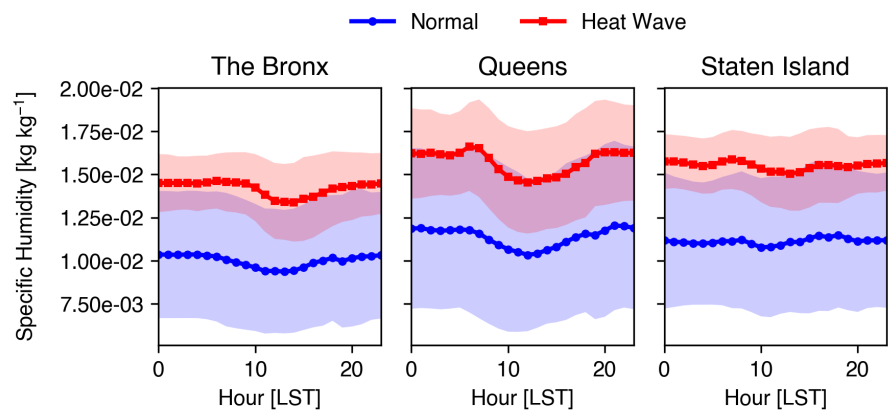


Figure 12: Anomalies of q during extreme heat events relative to the climatology at the surface.

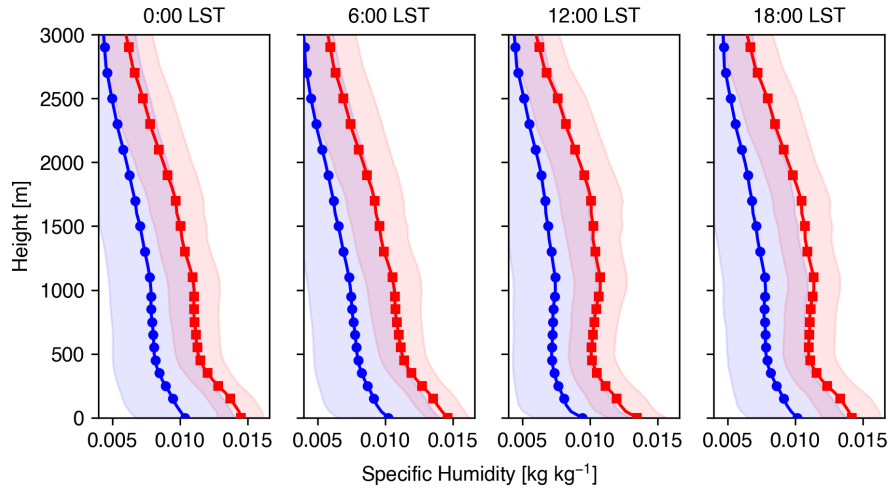


Figure 13: Vertical profiles of q in the Bronx during normal days (blue) and extreme heat events (red).

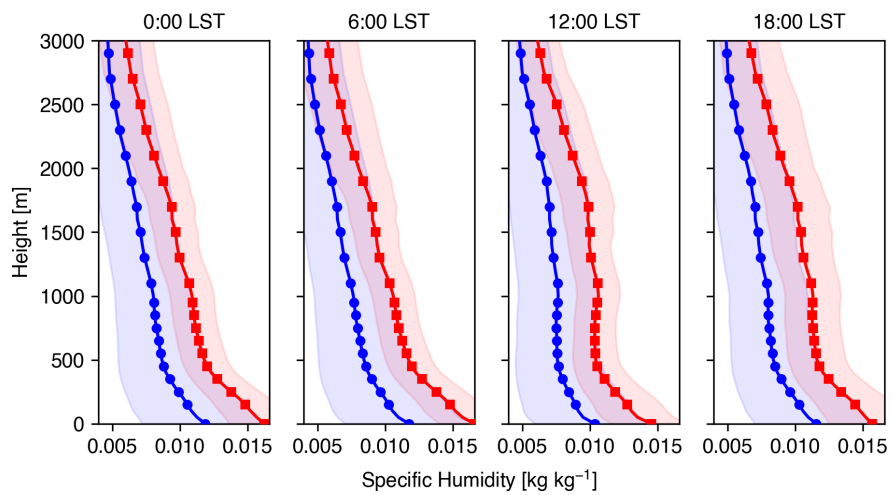


Figure 14: Vertical profiles of q in Queens during normal days (blue) and extreme heat events (red).

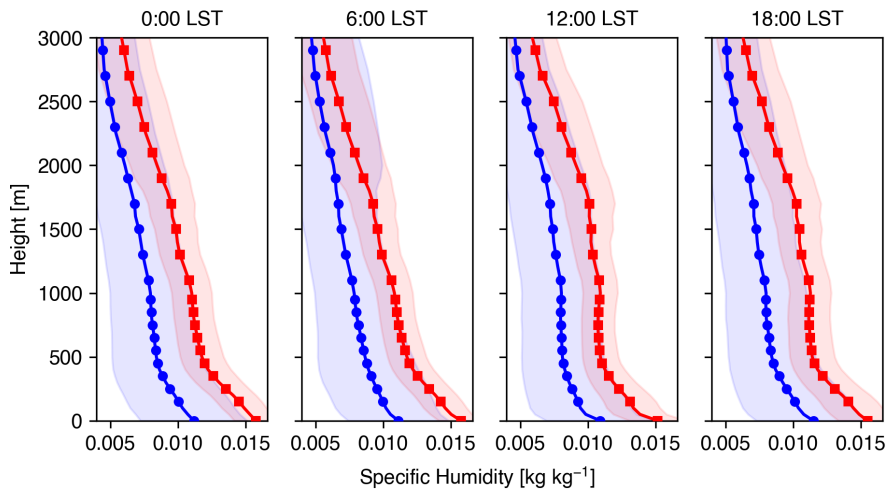


Figure 15: Vertical profiles of q in Staten Island during normal days (blue) and extreme heat events (red).

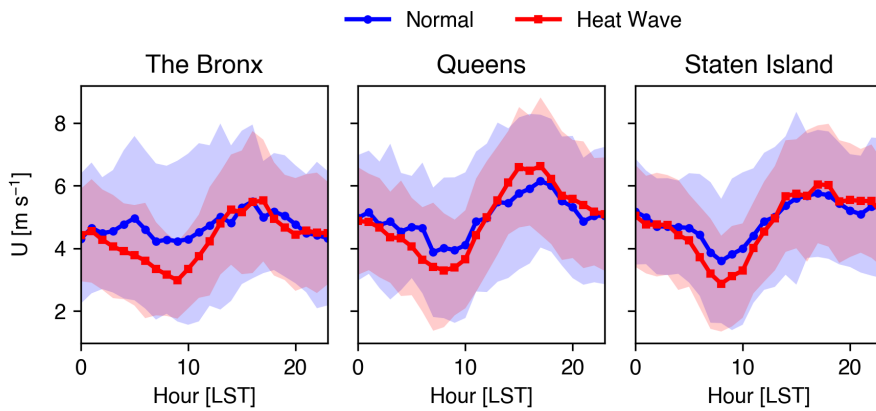


Figure 16: Anomalies of low-level U during extreme heat events relative to the climatology.

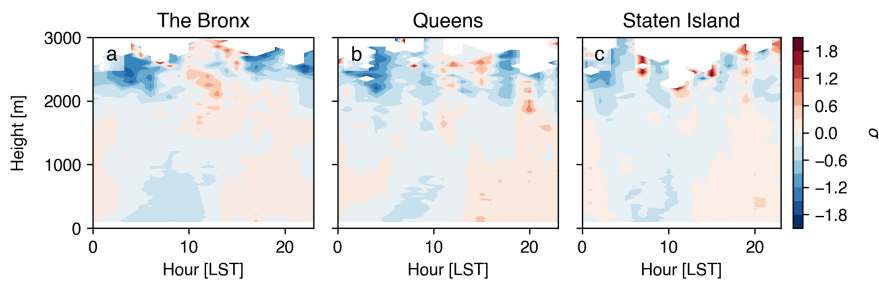


Figure 17: Anomalies of U during extreme heat events relative to the climatology over the urban boundary layer.

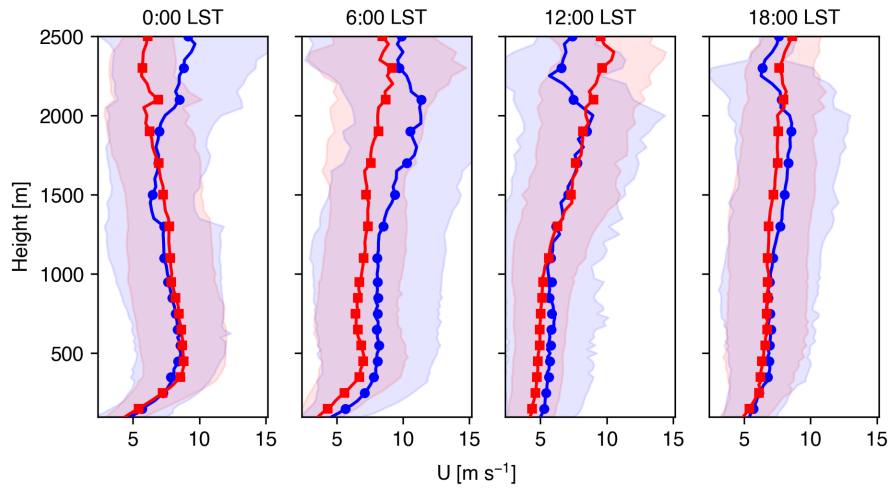


Figure 18: Vertical profiles of U in the Bronx during normal days (blue) and extreme heat events (red).

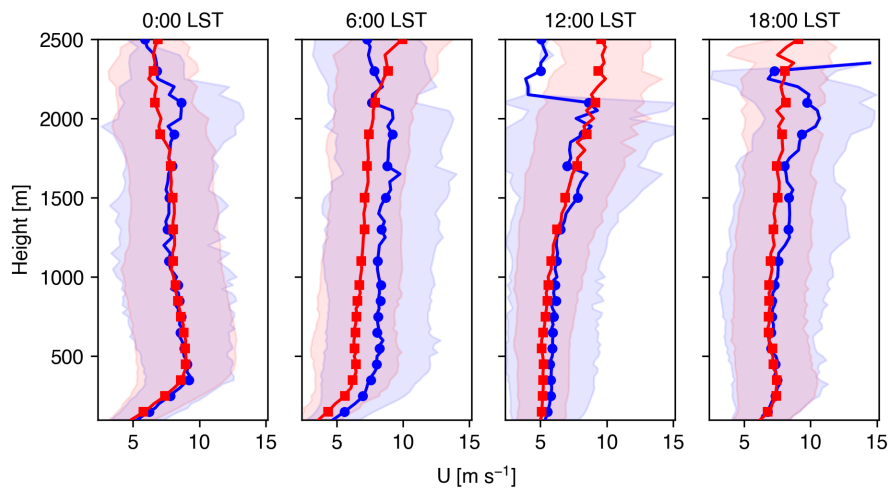


Figure 19: Vertical profiles of U in Queens during normal days (blue) and extreme heat events (red).

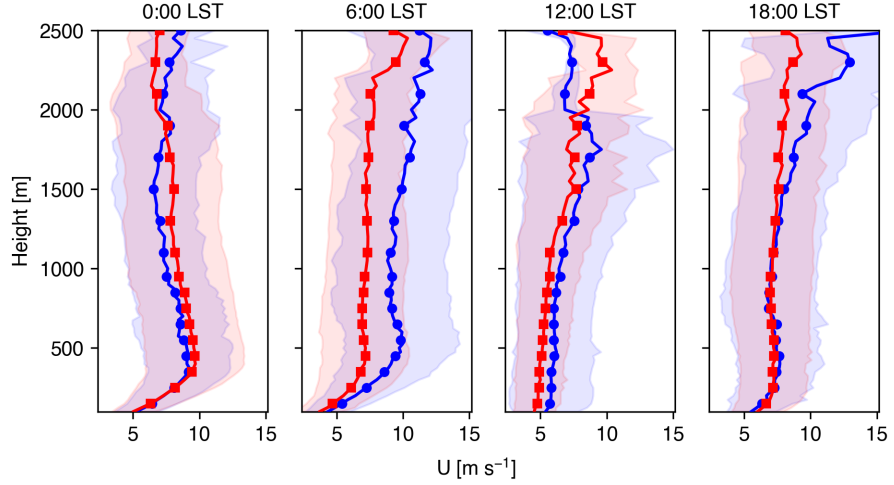


Figure 20: Vertical profiles of U in Staten Island during normal days (blue) and extreme heat events (red).

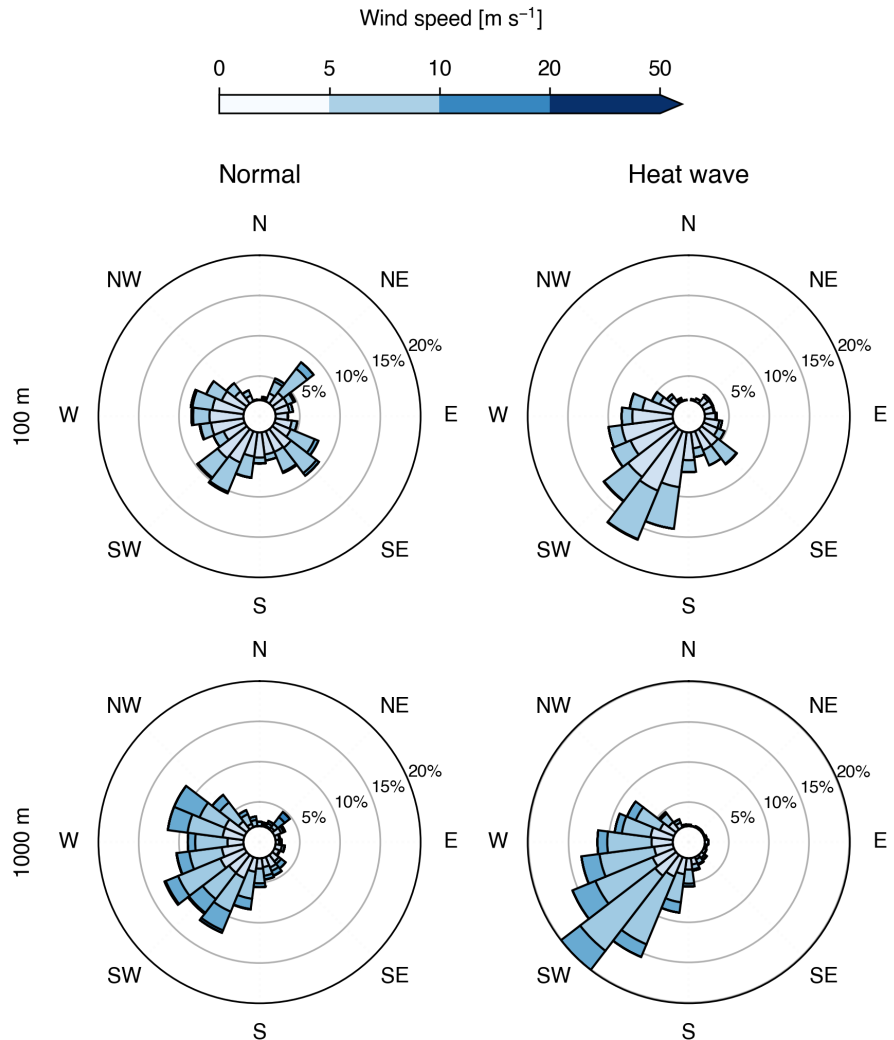


Figure 21: Horizontal winds in the lower-level (100 m) and mid-level of the urban boundary layer over the Bronx.

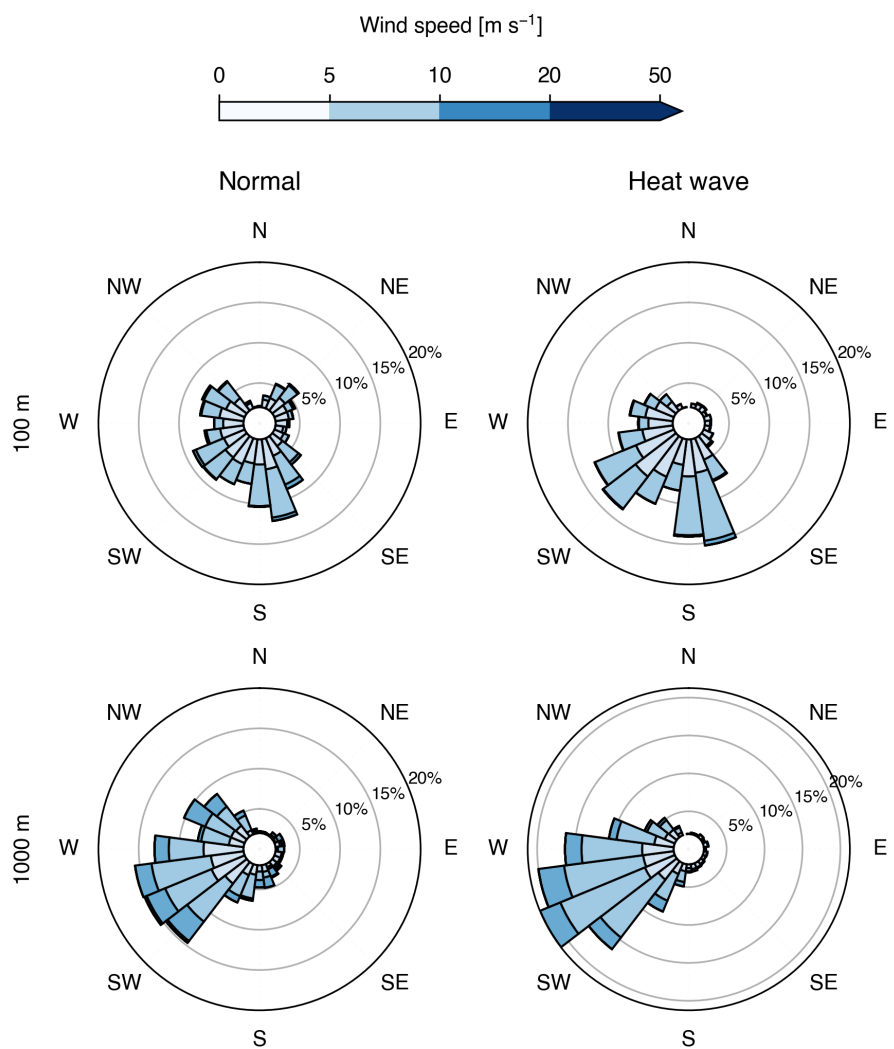


Figure 22: Horizontal winds in the lower-level (100 m) and mid-level of the urban boundary layer over Queens.

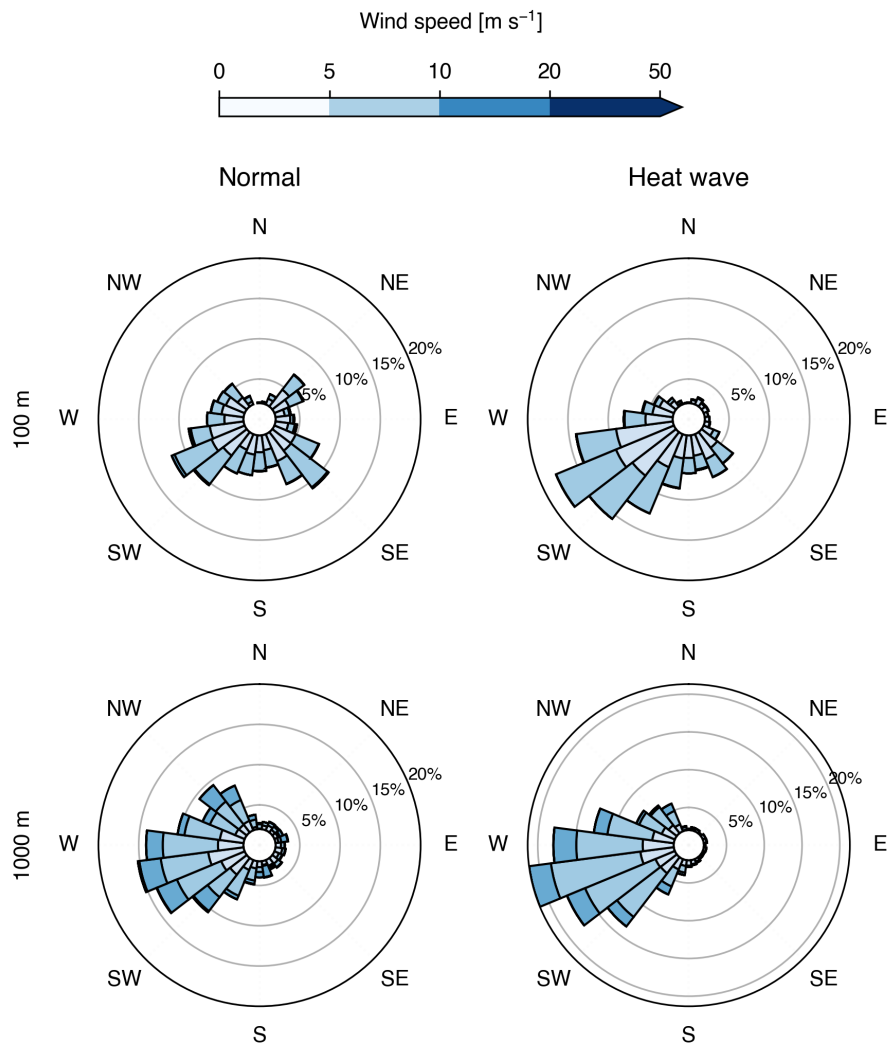


Figure 23: Horizontal winds in the lower-level (100 m) and mid-level of the urban boundary layer over Staten Island.

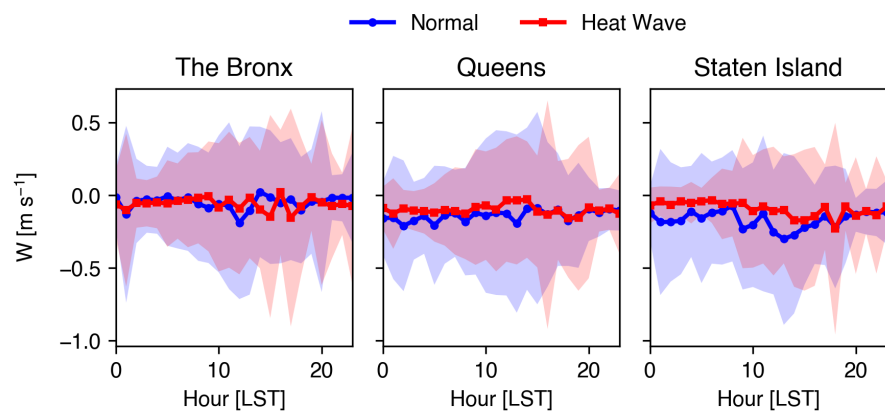


Figure 24: Anomalies of low-level w during extreme heat events relative to the climatology.

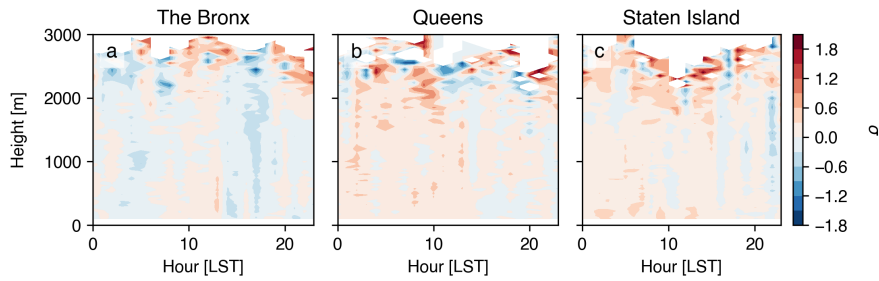


Figure 25: Anomalies of w during extreme heat events relative to the climatology over the urban boundary layer.

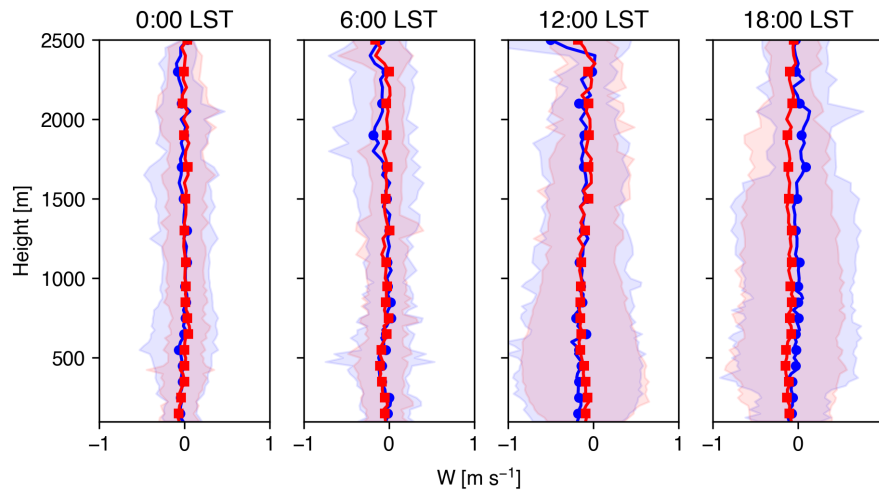


Figure 26: Vertical profiles of w in the Bronx during normal days (blue) and extreme heat events (red).

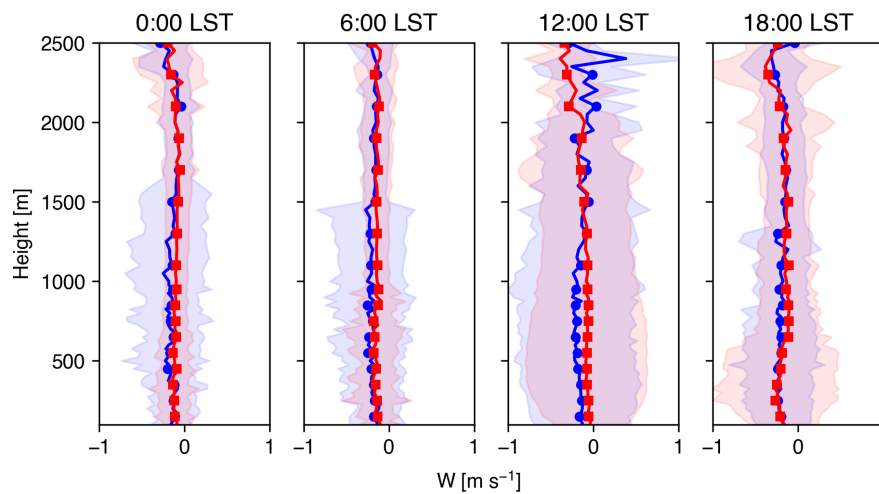


Figure 27: Vertical profiles of w in Queens during normal days (blue) and extreme heat events (red).

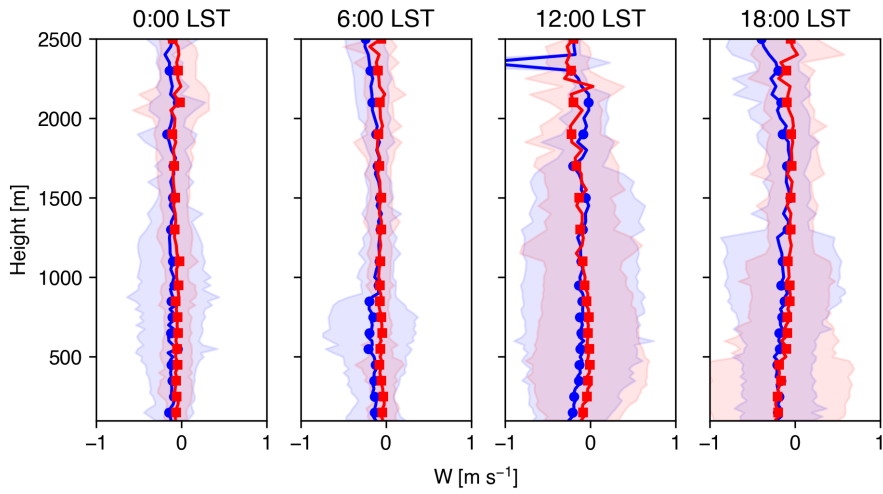


Figure 28: Vertical profiles of U in Staten Island during normal days (blue) and extreme heat events (red).

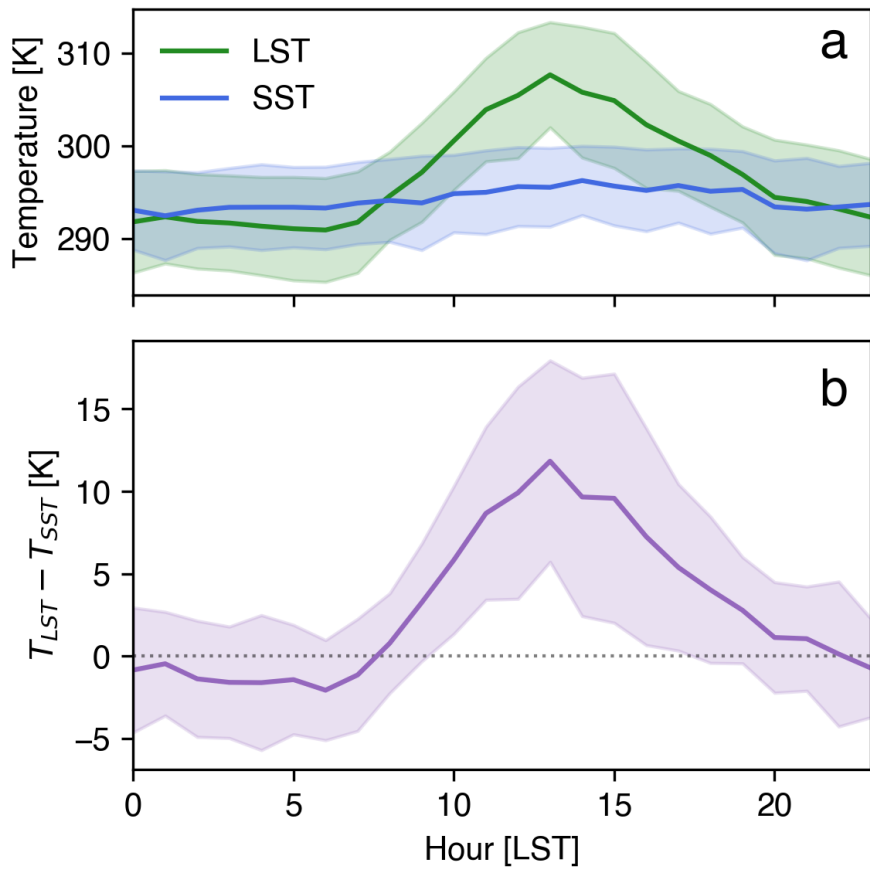


Figure 29: Temperature difference between Queens and New York Bight.

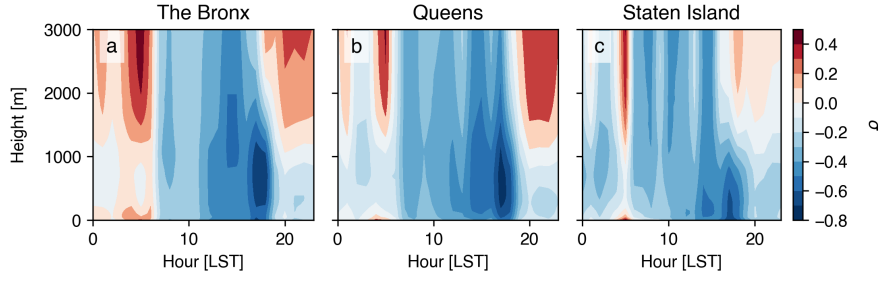


Figure 30: Anomalies of θ for normal days with a sea breeze relative to normal days without a sea breeze.

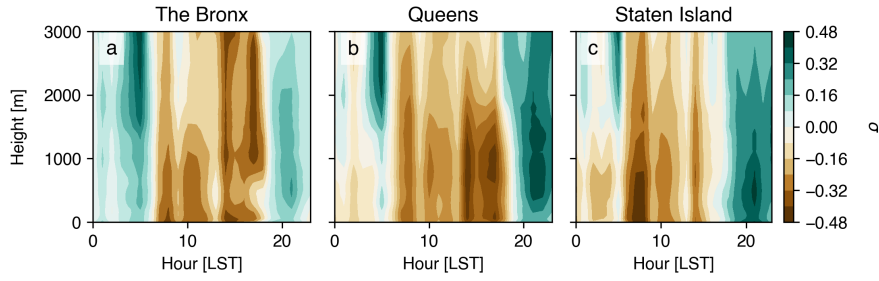


Figure 31: Anomalies of q for normal days with a sea breeze relative to normal days without a sea breeze.

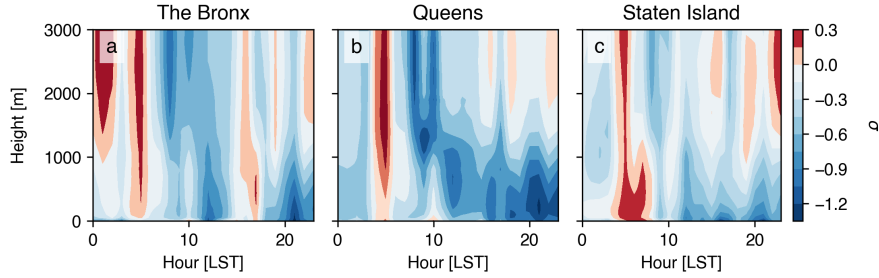


Figure 32: Anomalies of θ for heat wave days with a sea breeze relative to heat wave days without a sea breeze.

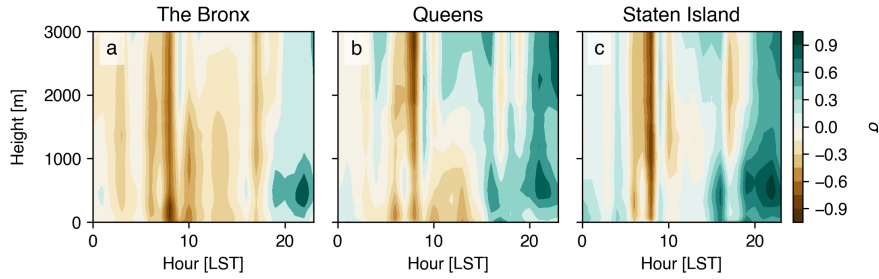


Figure 33: Anomalies of q for heat wave days with a sea breeze relative to heat wave days without a sea breeze.

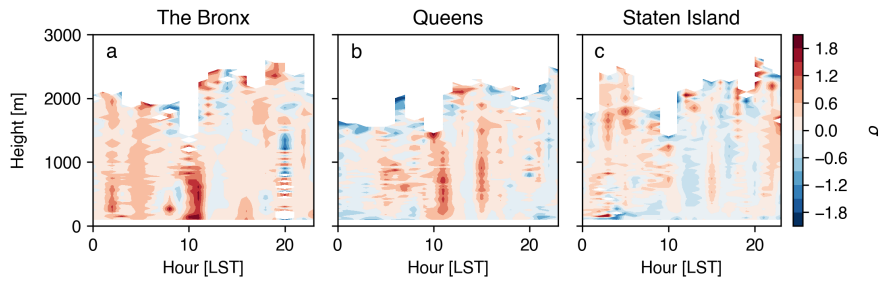


Figure 34: Anomalies of w for heat wave days with a sea breeze relative to heat wave days without a sea breeze.

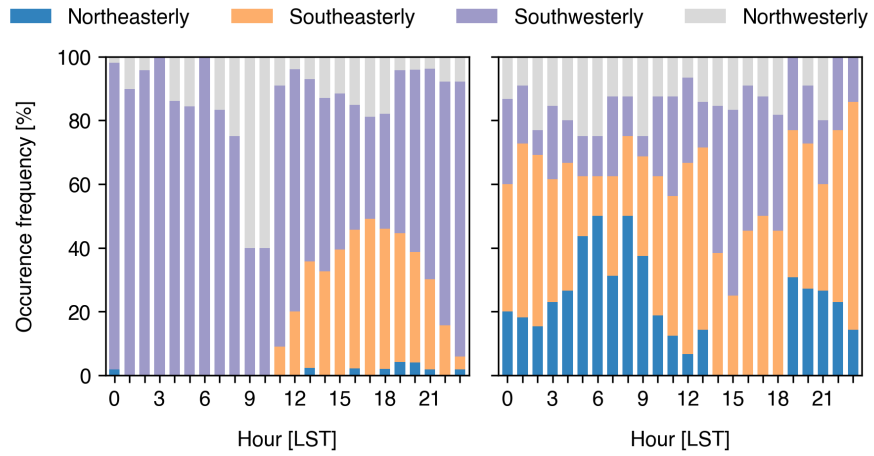


Figure 35: Occurrence frequency of wind directions at 100 m in the Bronx.

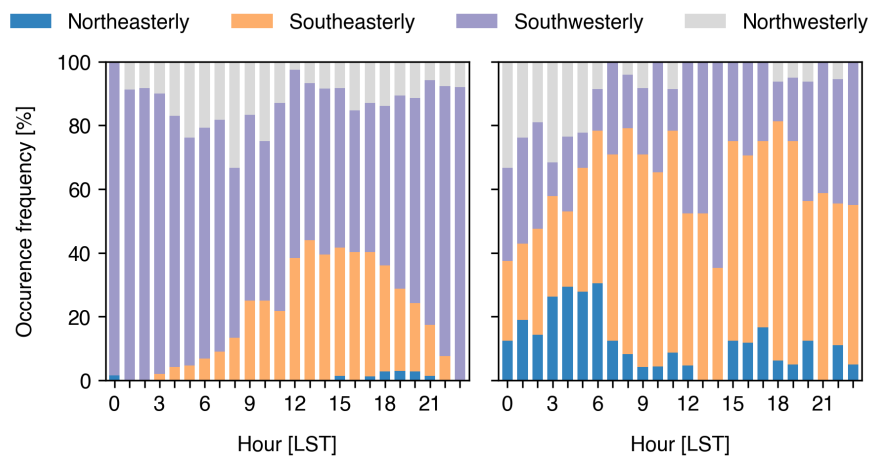


Figure 36: Occurrence frequency of wind directions at 100 m in Queens.

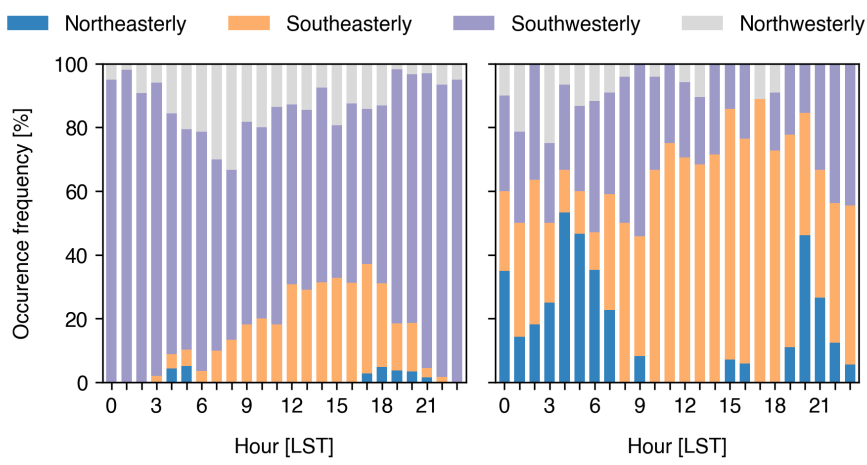


Figure 37: Occurrence frequency of wind directions at 100 m in Staten Island.